CrossMark

Remarkable impact of Ni²⁺ ion on the structural, optical, and magnetic properties of hexagonal wurtzite ZnS nanopowders

D. A. Rayan[1] · A. M. Elseman[1] · M. M. Rashad[1]

Abstract

Ni-substituted zinc sulfide $Zn_{1-x}Ni_xS$ ($x = 0.0$–0.8) nanopowders have been purposefully assembled using hydrothermal strategy based on inexpensive chloride salts and thiourea as sulfur sources. By X-ray diffraction, a hexagonal wurtzite structure with preferential orientation along the (0 0 8) plane was recognized at hydrothermal temperature 150 °C for period 24 h with nickel ion content. However, binary ZnS/Ni_3S_4 nanocomposites were identified by enhancing the nickel molar ratio up to 0.2–0.3 (20–30%). Whereas, ternary $ZnS/Ni_3S_4/NiS$ nanocomposites were accomplished by increasing Ni ion molar ratio in the range from 0.4 to 0.8. The microstructure of the Ni replaced ZnS particles from 0.0 to 0.6 exhibited microspheres like structure and with increasing the Ni^{2+} ion concentration, the microspheres converted to three-dimensional layers. The optical band-gap energy was slightly reduced from 3.39 to 3.32 eV with increasing the Ni ion addition from 0.1 to 0.3. Otherwise, two band-gap energies were existed to be 3.16–1.60 and 2.95–1.45 eV at Ni^{2+} ion substitution 0.60 and 0.80 molar ratios, respectively. Photoluminescence spectra measurements indicated that pure and Ni ion-substituted ZnS (0.1 and 0.2 molar ratios) were manifested three emission bands in the ranges of strong UV emission peak 350–375 nm with the weakest blue UV emission band 375–387 nm and the broadband visible emission at 400–600 nm. Eventually, weak ferromagnetic behavior was evidenced for different Ni^{2+}-substituted ZnS. The saturation magnetization was found to be maximum value of M_s of 0.33 emu/g as the result of improving the crystallization of cubic polydymite Ni_3S_4 structure at nickel ratio of 0.3.

1 Introduction

The concentration on the correlation between the magnetic and optical properties of diluted magnetic semiconductors (DMS) nanopowders has a considerable much scientific and technological concern due to the prospective applications in spintronics [1–3]. Semiconductor technologies are greatly developed since the 1970s using only the charge of the carrier. With the intriguing aspect, scientists expect with the manifestation of DMS that spintronics devices with monitoring both the charge and the spin of carriers can introduce a revolution to the semiconductor industry [4]. Interestingly, wide applications are predestined in spintronics biological labels, LEDs, lasers, bio-photonics, cellular, and biological labels [5–10]. In this context, semiconductor materials are doped with external impurity elements to improve the optical and the magnetic properties [4]. By doping with

the external impurity element, fine band-gap tuning can be achieved to enhance the magnetic and optical properties.

In particular, the astonishing changes in the nanoscale DMS are due to their quantum confinement effects. They have high optical and magnetic properties imputed to their hybrid nature, and hence, the concept of dilute magnetic semiconductors has emerged in the due course. Among these semiconductors, zinc sulfide is an imperative semiconductor compound of the II–VI groups known as quantum dots (QDs), with significant enforcement in the electronics and the optoelectronics devices on basis the wide direct band-gap energy of 3.5–3.7 eV at room temperature, excellent transport properties, high chemical stability, non-toxicity as well as low-energy fundamental phonon modes [11, 12]. The unique integration of these features distinguishes ZnS as essential candidate for solid-state solar cell windows, production of hydrogen, light-emitting applications, blue-light diodes, electro-luminescent displays, optical coatings, antireflection coating for infrared devices, electro-optic modulators, photoconductors, optoelectronics, catalysis, fluorescence imaging, tumour therapy field effect transistors, transducers, and sensors [13–18].

✉ M. M. Rashad
  rashad133@yahoo.com

[1] Central Metallurgical Research and Development Institute, P.O. Box 87, Helwan 11421, Egypt

It is known that ZnS exists in two different crystal structures involved stable cubic form recognized as zinc blende or sphalerite, whereas the hexagonal framework is renowned as wurtzite both of which have the same band-gap energy and the direct band structure [17]. Evidently, the structural, morphology, the optical, and the magnetic performances are ultimately revolved on the synthesis strategies. Accordingly, diversified methodologies have been anticipated to synthesize ZnS including the single-source molecular precursor [14, 15], microemulsion [13], solvothermal and hydrothermal route [18, 19], and direct elemental reaction route [20]. In comparison, the hydrothermal method has been successfully utilized as a perfect route to prepare ZnS NPs with good homogeneity and confirm morphologies [21]. Otherwise, a number of reports dealing with the magnetic and the optical properties of ZnS NPs with different transition metals including Mn^{2+}, Co^{2+}, Ni, Cu^{2+}, and Cd^{2+} ions as well as rare-earth elements with many inconsistencies are available [22–26]. The substitution atomic ratios of TM ions are systematically exercised in the range from 1 to 10%.

From the best of our knowledge, the replacement of ZnS nanopowders with high ratio of Ni^{2+} ion from 30 to 80% is not mentioned elsewhere in the literature. Therefore, in the present article, an efficient and a low-cost hydrothermal methodology for the synthesis of Ni-doped ZnS nanopowders at the high atomic ratios (0.0–0.80) was examined on basis of cheap-starting materials. Besides, the impact of Ni^{2+} ion doping on the structural, microstructure as well as optical and magnetic properties was also explored. Overall, such work has great potential for industrial applications involving electronics and optoelectronics devices.

2 Experimental

2.1 Materials and methods

$Zn_xNi_{1-x}S$ nanoparticles have been tailored using a facile hydrothermal strategy based on low-cost starting materials. Inexpensive chloride salts of analytical grade involved zinc chloride $ZnCl_2$, nickel chloride $NiCl_2$ as well as thiourea $(NH_2)_2CS$ as sulfur were utilized. Moreover, high-purity water with a resistivity of 18.2 MΩ/cm was used for the preparation of all aqueous solutions. In a typical procedure, 0.1–x mole zinc chloride, x mole nickel chloride (x from 0.0 to 0.80), and 0.1 mol thiourea powders were added into a Teflon-lined autoclave with the capacity of 50 ml, which was filled with 40 ml de-ionized water. After that, the autoclave was sealed and maintained at 150 °C for 24 h. Thus, the autoclave was allowed to cool to room temperature naturally. The produced yellow precipitates were filtered then washed by de-ionized water and absolute alcohol several times.

Finally, the precipitates were dried at 100 °C overnight to form nanoparticles.

2.2 Physical characterization

X-ray powder data were realized by a Brucker axis D8 diffractometer with crystallographic data software Topas 2 using Cu–K_α ($\lambda = 1.5406$ Å) radiation operating at 40 kV and 30 mA at a rate of 2°/min. The microstructures of nanocrystalline powders were considered using a scanning electron microscopy (SEM) (JSM-5400). The UV–Vis absorption and diffuse reflectance spectrum were implemented at room temperature using UV–Vis–NIR spectrophotometer (Jasco-V-570 spectrophotometer, Japan) fitted with integrating sphere reflectance unit (ISN) in the wavelength range 200–2000 nm. Photoluminescence (PL) spectra were recorded at room temperature with a fluorescence spectrophotometer equipped with a 50 W xenon lamp (Shimadzu RF-5301PC, Kyoto, Japan). The magnetic properties of the synthesized samples were proceeded at room temperature using a VSM (7410-LakeShore, USA) in a maximum applied field of 20 kOe. From the obtained hysteresis loops, the saturation magnetization M_s, remanence magnetization M_r and coercivity H_c were estimated.

3 Results and discussion

In this article, the $Zn_xNi_{1-x}S$ nanoparticle was utilized using a facile hydrothermal strategy based on low-cost starting materials. The scheme and technique which used the reaction of starting materials with autoclave hydrothermal are appeared in Fig. 1. It can be seen that a mixture of zinc chloride, nickel chloride, and thiourea was injected to the autoclave by one step. Then, a sigma bond of $Zn_xNi_{1-x}S$ has been collected and the spherical structure wad shaped. These spherical particles were consolidated together and the target materials were achieved under 150 °C for 24 h.

3.1 Crystal structure

Figure 2a shows the XRD profile for the precursor formed from the treatment of zinc chloride and thiourea hydrothermally treated at 150 °C for 24 h. Evidently, the results revealed that the undoped ZnS particles (JCPS # 72-0162) with peaks' positions at (1 0 2), (1 0 3), (0 0 10), (1 0 4), (1 1 0), (2 0 3), and (1 1 10) were recognized as a hexagonal wurtzite phase. Meanwhile, Fig. 2b depicts the phases' evolution after subrogated ZnS nanoparticles by different concentrations of Ni^{2+} ions ($x = 0.05$, 0.10, 0.20, 0.30, 0.40, 0.60, and 0.80). Obviously, wurtzite ZnS phase was disclosed with Ni^{2+} ion content of 0.05 and 0.10. Remarkably, cubic polydymite Ni_3S_4 (JCPS # 47-1738) structure
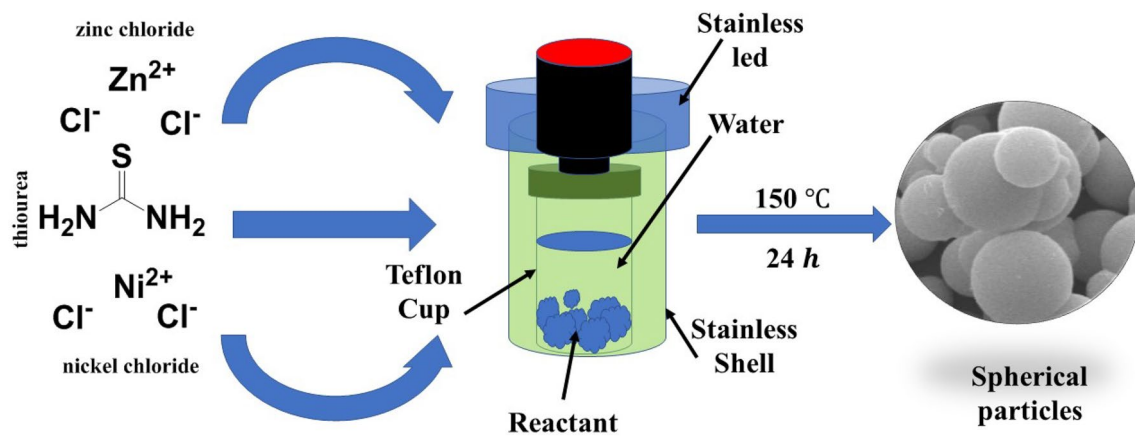
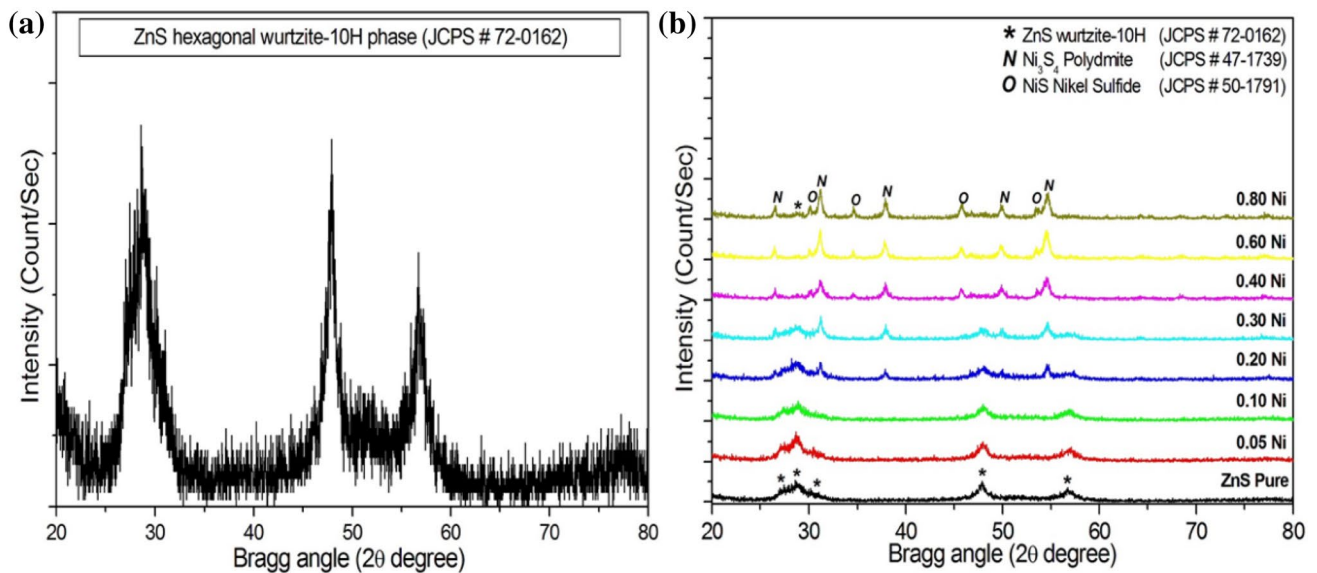**Fig. 1** Possible reaction of $Zn_xNi_{1-x}S$ by autoclave hydrothermal under 150 °C for 24 h

Fig. 2 a X-ray diffractions of pure ZnS at 150 °C for 24 h, **b** X-ray diffraction profiles of Ni²⁺-substituted ZnS nanoparticles at different Ni²⁺ concentrations from 0.0 to 0.80 hydrothermally treated at temperature 150 °C for time 24 h

was demonstrated as a secondary phase with Ni²⁺ molar ratios of 0.2 and 0.3. Furthermore, hexagonal NiS (JCPS # 50-1791) was matched with ZnS and Ni_3S_4 phases at high Ni content from 0.4 to 0.8 molar ratios. The crystallite size was estimated from the most intense peak of each phase based on Debye–Scherrer formula [27–29]:

$$d_{RX} = k\lambda/\beta\cos\theta, \tag{1}$$

where d_{RX} is the crystallite size, $k = 0.9$ is a correction factor related to the account for particle shapes, β is the full-width at half-maximum (FWHM) of the most intense diffraction peak plane, λ is the wavelength of Cu target $= 1.5406$ Å, and θ is the Bragg angle.

Table 1 records the change in the crystallite size with Ni²⁺ ion content. Clearly, the crystallite size of the obtained pure ZnS nanopowders was found to be 21.5 nm for the precursor formed from the treatment of zinc chloride and thiourea hydrothermally treated at 150 °C for 24 h. However, the crystallite size for ZnS phase was seemed to reduce with increasing the addition of Ni²⁺ ion. In this vein, the crystallite size was decreased from 21.5 nm for pure ZnS to 3.0 nm with further increasing the Ni²⁺ ion molar ratio up to 0.8. Otherwise, the crystallite sizes of Ni_3S_4 and NiS phases were found to increase with the similar trends with increasing the concentration of nickel ion. The lattice parameters (*a*

Table 1 Variation of phase evolution, crystallite size, lattice parameters, cell volume and X-ray density of Ni^{2+} substituted ZnS nanoparticles at different Ni^{2+} concentrations from 0.0 to 0.80 hydrothermally treated at temperature 150 °C for time 24 h

Ni doped (molar ratio)	Phases	Cry. size (nm)	a (Å)	c (Å)	Cell volume (Å³)	Theoretical density, ρ_x (g/cm³)
0.00	ZnS	21.5	3.667	31.598	424.896	3.046
0.05	ZnS	10.7	3.669	31.565	425.058	3.045
0.10	ZnS	8.2	3.670	31.554	424.913	3.046
0.2	ZnS	7.1	3.671	31.598	425.493	3.042
	Ni_3S_4	20.1	9.490	–	854.668	4.730
0.3	ZnS	7.0	3.667	31.598	424.896	3.046
	Ni_3S_4	20.9	9.491	–	854.892	4.729
0.4	ZnS	3.0	3.669	31.565	425.058	3.045
	Ni_3S_4	21.1	9.495	–	855.905	4.723
	NiS	27.9	3.414	5.343	62.283	4.839
0.6	ZnS	3.0	3.667	31.565	424.461	3.050
	Ni_3S_4	26.4	9.509	–	859.723	4.702
	NiS	29.0	3.431	5.322	62.638	4.812
0.8	ZnS	3.0	3.669	31.576	425.203	3.044
	Ni_3S_4	28.2	9.499	–	857.027	4.717
	NiS	33.4	3.425	5.316	62.347	4.834

and c) of the samples were calculated using the following equations [30–32]:

$$\frac{1}{d_{hkl}^2} = \frac{4}{3}\left(\frac{h^2 + hk + k^2}{a^2}\right) + \frac{l^2}{c^2} \quad \text{ZnS and NiS hexagonal structure,} \tag{2}$$

$$\frac{1}{d_{hkl}^2} = \frac{h^2 + k^2 + l^2}{a^2} \quad \text{polydymite } Ni_3S_4 \text{ cubic structure,} \tag{3}$$

where a, b, and c were the lattice parameter, d is the interplanar distance, and (hkl) are the Miller indices. The unit cell volume V of pure and Ni-substituted ZnS nanopowders were calculated using the equation [30–33]:

$$V = a^2c \quad \text{ZnS and NiS hexagonal structure} \tag{4}$$

$$V = a^3 \quad \text{polydymite } Ni_3S_4 \text{ cubic structure.} \tag{5}$$

The theoretical density was estimated using the equation [33]:

$$\rho_x = \frac{\sum A}{N_A V}, \tag{6}$$

where ρ_x is the X-ray theoretical density, A is the sum of the atomic weights of all the atoms in the unit cell, and N_A is the Avogadro's number. Table 1 reports the change in the lattice parameters, unit cell volume, and theoretical X-ray density. It can be seen that the theoretical density was increased with Ni^{2+} ion content. In particular, it is well known that Ni ionic radius (0.078 nm) is smaller than Zn ionic radius (0.082 nm). Subsequently, the lattice expansion is weakened if Zn ions

are replaced by nickel ions with a smaller radius. The weakening of the lattice expansion results in slight decrease in lattice parameter (a) with increasing nickel content.

3.2 Microstructure

Figure 3 displays the SEM morphologies of pure and Ni-doped ZnS samples synthesized at different Ni^{2+} ion ratios hydrothermally treated at 150 °C for 24 h. Apparently, SEM micrograph of the pure ZnS sample exhibited microspheres with different aggregates because of their large surface-to-volume ratio. The average grain sizes of undoped ZnS particles were about 1–2 μm. However, the microspheres were constructed of layers which they formed by the aggregation of Ni-doped ZnS nanoparticles in three dimensions. These layers were clearly seen at a high concentration of Ni ion, as described in Fig. 3. It is known that the application of the materials was highly correlated with its morphology and size. Among these fabrication techniques, the hydrothermal route offers an advantage in tailoring the product morphology and size [34]. Herein, the phases of ZnS nanoparticles doping by different concentrations of Ni^{2+} ions ($x = 0.05$, 0.10, 0.20, 0.30, 0.40, 0.60, and 0.80) have been effect on the morphology and particles' sizes. There has been systematic investigation into how this doping concentration affects $Zn_xNi_{1-x}S$ crystals, though several different morphologies are based on the hydrothermal route. To understand the mechanism of particle growth, the energy is redistributed between a particle and the surrounding media under temperature and controlled time. As shown experimentally in Fig. 1, it is possible to suppose that the particle heating–melting evaporation mechanism could be applicable for spherical

nanoparticle formation. Meanwhile, the energy absorbed by a particle from the hydrothermal is spent for the particle solidification processes. It is seen that the sample morphology and size are highly dependent on the Ni^{2+} concentration. When adding small amounts of Ni^{2+} in a range of 0.05–0.20 molar ratio, the prepared samples mainly consist of sphere-like structures without impurities, as shown in Fig. 3. The concentration ratio (0.30–0.80) exhibits irregular sphere-like structures, and their size increases with the increase in Ni^{2+} content.

3.3 Optical properties

3.3.1 UV absorption characteristics

The optical properties of $Zn_{1-x}Ni_xS$ ($x = 0$, 0.1, 0.3, 0.6, and 0.8 molar ratio) nanopowders were examined using UV–Vis–NIR spectrophotometer using integrating sphere unit over the wavelength range 200–1300 nm. Figure 4 shows the optical diffuse reflectance and the absorbance spectra of pure and Ni ion-substituted ZnS nanopowders with different Ni^{2+} ion molar ratios. Remarkably, pure ZnS exhibited the high optical reflectivity of around 75–78% in the infrared and visible regions, as presented in Fig. 4a. Further increasing in the Ni-substituted ZnS nanopowders resulted in the smallest reflective with the average reflectivity of around 35–13% for Ni-substituted 0.1 and 0.8 molar ratios, respectively. Figure 4b shows the obvious absorption edge at about 365 nm for undoped ZnS nanoparticles, which was not close to the peak of bulk ZnS is expected at 337 nm ($E_g = 3.68$ eV) [11, 12], and the maximum absorbance maximum was about 320 nm. This large blue shift could be attributed to the combined effect of optical transition to the excitonic state (transition from the top of the valence band to the bottom of the conduction band) of the synthesized nanoparticles. Ni doping shifts the absorption onset to blue 375–380 nm (from 3.35 to 3.26 eV) of Ni-doping level from 0 to 0.8 molar ratio in addition to the visible light absorption band with the onset around 540 nm, indicating a decrease in the bandgap. However, the absorbance band of Ni-doped ZnS nanoparticles was dominated at the visible region by the Ni d–d transitions, which Ni with T_d site symmetry is allowed by the electric dipole selection rule and is very intense. However, the energy transitions levels of Ni^{2+} came from the ground state $^3A_1(F)$ to the excited states $^3T_2(F)$, $^3A_2(F)$, $^3T_1(P)$, and $^3T_1(G)$ [35].

In the limiting case of an infinitely powder samples, thickness and sample holder have no influence on the value of reflectance (R). In this case, the reflectivity R can be transformed into a value proportional to the absorption using the Kubelka–Munk function [36–39]:

$$F(R\infty) = (100 - R)/(2R). \tag{7}$$

$F(R\infty)$ is the so-called remission or Kubelka–Munk function. In the parabolic band structure, the bandgap E_g,

and the absorption coefficient α, of a direct band-gap semiconductor are related through the well-known equation [36]:

$$\alpha h\nu = A(h\nu - E_g)^{1/n}, \tag{8}$$

where α is the linear absorption coefficient of the material, $h\nu$ is the photon energy, and A is proportionality constant. When the material scatters in perfectly diffuse manner (or when it is illuminated at $60\pm$ incidence), the K–M absorption coefficient K becomes equal to 2α ($K = 2\alpha$). In this case, considering the K–M scattering coefficient S as constant with respect to wavelength, and using the remission function in Eq. (4). we obtain the expression [36]:

$$(h\nu F(R\infty))^n = B(h\nu - E_g). \tag{9}$$

Plotting the Tauc plot of $[h\nu F(R\infty)]^n$ against $h\nu$ with $n = 2$ for the direct band-gap material to extract the bandgap energy of the different samples, as shown in Fig. 5a. Meanwhile, Table 2 summarizes the band-gap energy for pure ZnS and Ni-substituted NiS. It can be observed from the inset that as the increasing molar ratio of Ni^{2+} ion-doped ZnS, the band-gap energy converts to decrease from 3.39 to 3.32 eV with more increasing Ni^{2+} ion from 0.10 to 0.30 molar ratios. This change of the band-gap energy with incorporation of Ni ion into ZnS lattice was interpreted as mainly due to the sp–d exchange interactions between the band electrons and the localized d electrons as the results of Ni ion which is also considered as the blossoming of magnetic phase [40]. It is believed that the s–d and p–d exchange interactions lead to a negative and a positive correction to the conduction band as well as the valence band edges resulting in a band-gap narrowing [41]. Meanwhile, in high substitution Ni^{2+} ion at 0.60–0.80 molar ratios, the optical band-gap energy was doubled to be 3.16–1.60 eV and 2.95–1.45 for Ni^{2+} ion 0.6 and 0.8 molar ratios, respectively. The double band-gap energy was imputed to form of $ZnS/Ni_3S_4/NiS$ nanocomposites as the result of low optical band-gap energy for bulk $Ni_3S_4 \sim 2.7$ eV and slight optical band-gap energy for NiS ~ 0.8 eV [42, 43].

3.3.2 Photoluminescence (PL) spectroscopic characteristics

Figure 5b demonstrates the photoluminescence spectra of pure and Ni-substituted ZnS. Clearly, pure and Ni ion-substituted ZnS (0.1 and 0.2 molar ratios) displayed three emission bands in the ranges of strong UV emission peak 350–375 nm with the slight UV emission peak 375–387 nm and the broad band visible emission at 400–600 nm. The broad visible emission bands may be attributed to the recombination of electron hole induced by the change of local charge distribution at the defect sites [44]. Evidently, the intensity of the PL spectrum was found to reach the maximum with increasing Ni concentration from 0.1 to 0.2. However, the intensity of
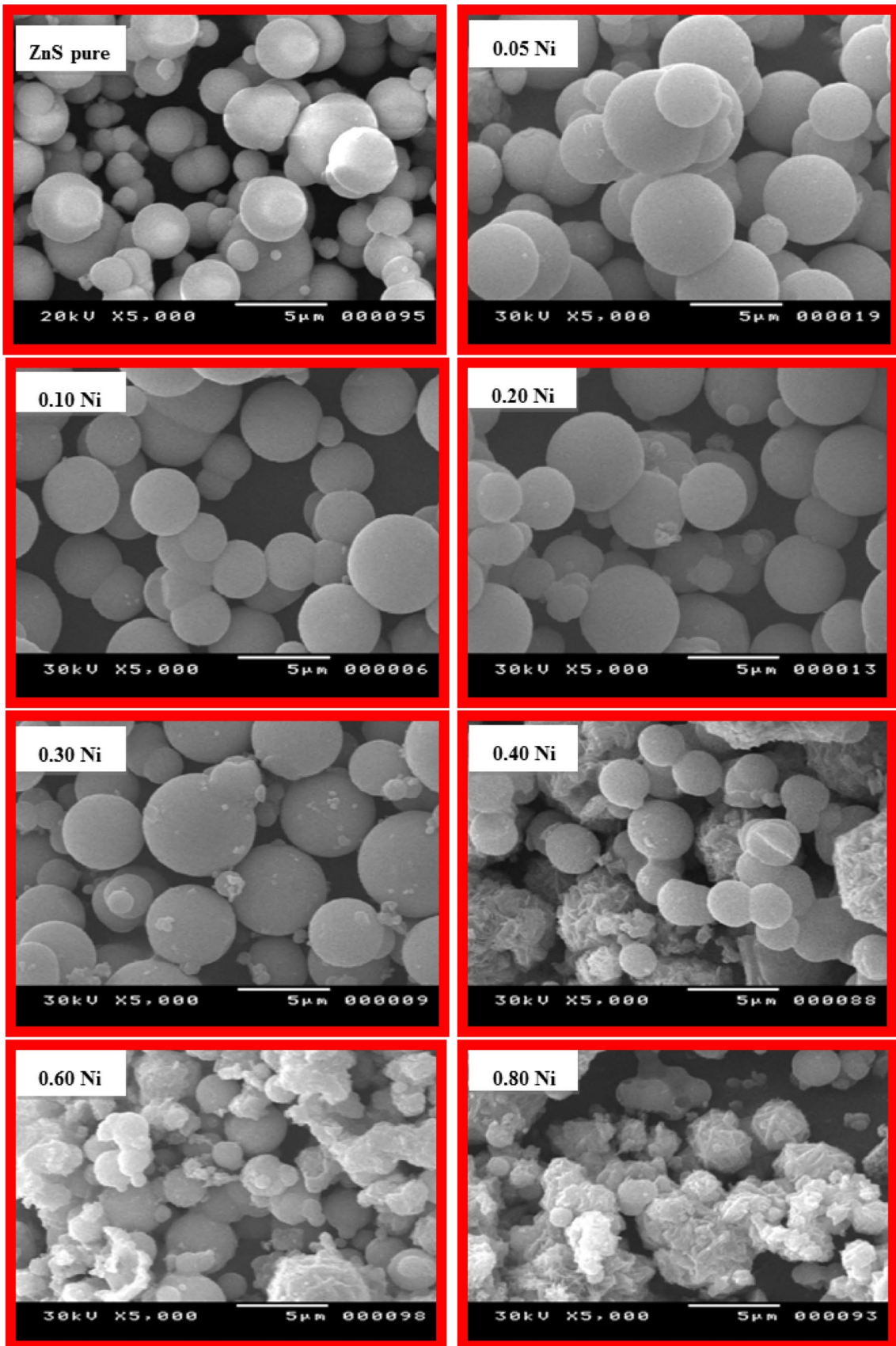
ZnS pure

20kV X5,000   5µm 000095

0.05 Ni

30kV X5,000   5µm 000019

0.10 Ni

30kV X5,000   5µm 000006

0.20 Ni

30kV X5,000   5µm 000013

0.30 Ni

30kV X5,000   5µm 000009

0.40 Ni

30kV X5,000   5µm 000088

0.60 Ni

30kV X5,000   5µm 000098

0.80 Ni

30kV X5,000   5µm 000093

samples was found to slightly decrease with the increasing of Ni amount until 0.6 molar ratio. Meanwhile, strong photoluminescence was observed at room temperature for the substituted samples suggesting the high efficiency of photon–electron and/ or the exciton coupling in the nanomaterials perhaps. Photoluminescence spectrums in the undoped ZnS as well as substituted samples were distinguished due to the inherent defects as cationic deficiency present in the material. The enhances the PL intensity with substitution Ni^{2+} ions substituted ZnS could increase the number of trapped electron hole pairs and emit more photons. The mechanism of PL emission was explicated on basis of the defects distributed- in ZnS nanostructures possessed of two parts: (I) the zinc vacancy (V_{Zn}) and the interstitial sulfur (I_S) atom as acceptor state as well as (II) the sulfur vacancy (V_S) and interstitial zinc (I_{Zn}) atoms as the local donor state [45]. Interstitial sulfur (I_S) states and zinc vacancies (V_{Zn}) should be located closer to the valence band edge; meanwhile, interstitial zinc (I_{Zn}) states and sulfur vacancies (V_S) should be located closer to the conduction band edge as well as energy levels of vacancies are deeper than interstitial states [46].

3.4 Magnetic properties

The magnetic properties were examined by vibrating sample magnetometer at room temperature in maximum applied magnetic field 20 KOe. M–H hysteresis loops of the produced pure and Ni-substituted ZnS samples are presented

in Fig. 6. The change in magnetic properties is summarized in Table 3. Plainly, all samples showed diluted magnetic semiconductor with weak ferromagnetic characteristics. The magnetic characteristics of undoped ZnS sample is imputed to sulfur vacancies and the stronger exchange interactions between these sulfur vacancies. It can be seen that the coercivity was very small, and the loops had very narrow shapes similar to ferromagnetic DMSs. The saturation magnetization (M_s), remanence magnetization (M_r) and the coercivity (H_c) values were found to increase with increasing Ni^{2+} ions content from 0.0 to 0.3. Otherwise, M_s, M_r and H_c values were decreased with enhancing the Ni^{2+} ions content from 0.4 to 0.8 with Ni concentration from 0.0 to 3.0 with regular spherical structure, the local density of states at the Fermi level increases and exchange interaction is enhanced leading to enhance ferromagnetism. the origin of magnetism in the samples is attributed the exchange interaction between local spin-polarized electrons from the electrons of Ni^{2+} ions and the conductive electrons. Consequently, such interaction can lead to the spin polarization of conductive electrons. Then, the spin-polarized conductive electrons undergo an exchange interaction with local spin-polarized electrons of other Ni^{2+} ions. Thus, after a successive long-range exchange interaction, almost all Ni^{2+} ions exhibit the same spin direction, resulting in enhancement of the saturation magnetization of the samples [47]. Meanwhile, to have a better perspective of these changes, the magnetic parameters can be dependence on to their difference in nanocomposites of ZnS/Ni$_3$S$_4$/NiS, where the different anisotropies, domains, and numbers of surfaces within the nanocrystals play an essential role in the magnetic properties of the nanocomposites [48]. Firstly, at Ni^{2+} ions content from 0.05 to 0.3 molar ratios, M_s, M_r and
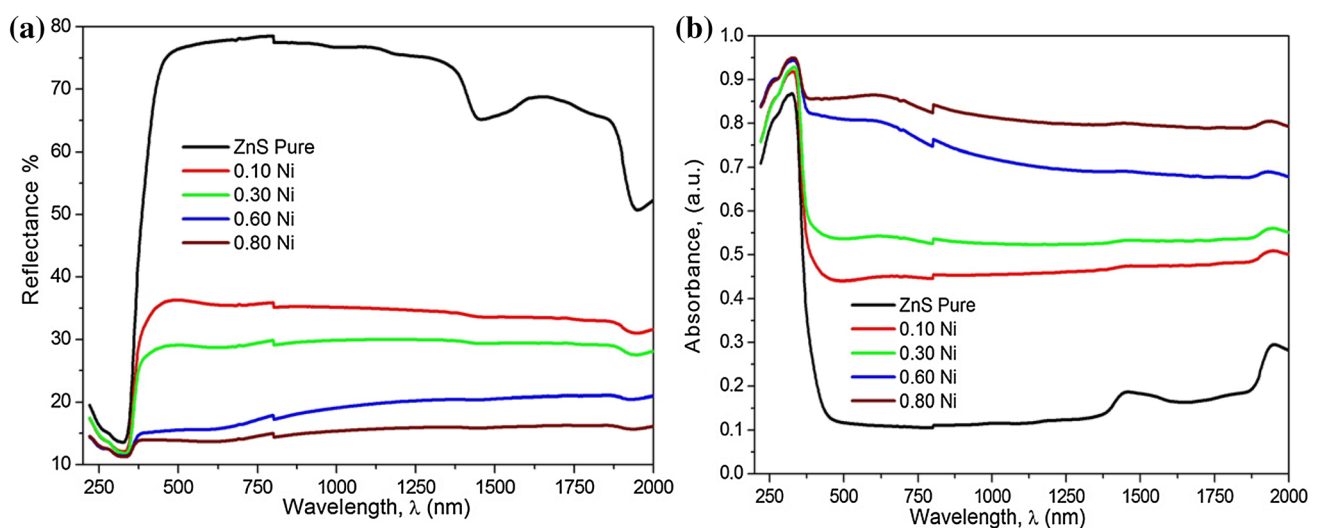

Fig. 4 **a** Reflectance (*R*) and **b** absorbance (*A*) of Ni^{2+}-substituted ZnS nanoparticles at different Ni^{2+} concentrations from 0.0 to 0.80 hydrothermally treated at temperature 150 °C for time 24 h
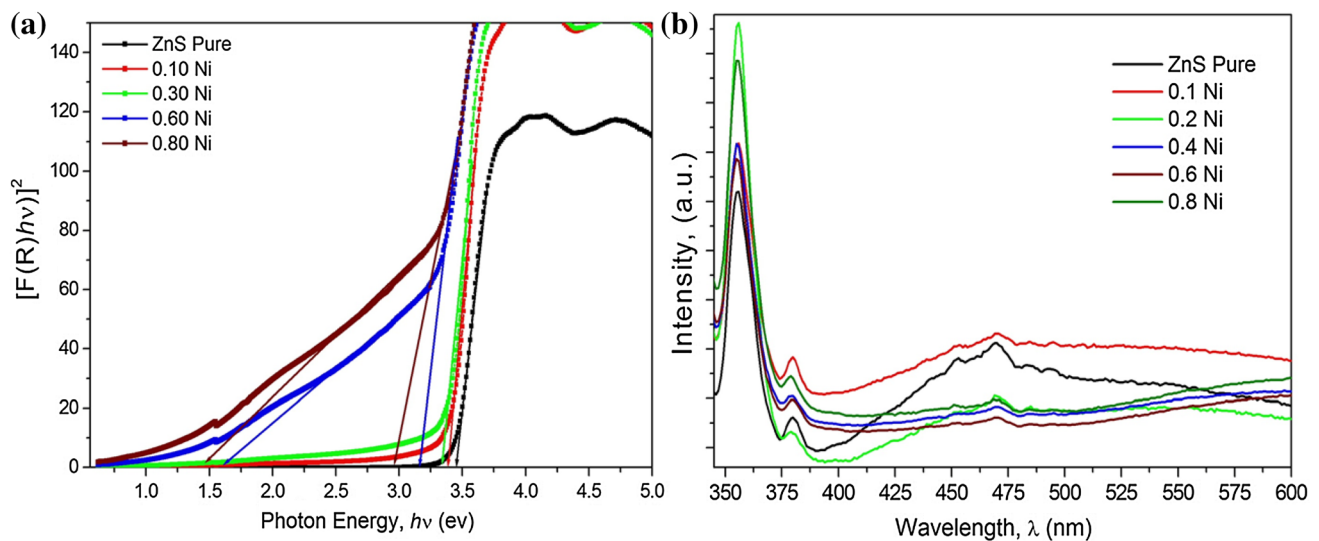
Fig. 5 **a** $(\alpha h\nu)^2$ versus photon energy ($h\nu$). **b** Photoluminescence spectra of Ni^{2+} substituted ZnS nanoparticles at different Ni^{2+} concentrations from 0.0 to 0.80 hydrothermally treated at temperature 150 °C for time 24 h

Table 2 Variation of the crystallite size and band-gap energy of Ni^{2+} substituted ZnS nanoparticles at different Ni^{2+} concentrations from 0.0 to 0.80 hydrothermally treated at temperature 150 °C for time 24 h

Ni substituted (molar ratio)	Phases	Cry. size (nm)	Optical band-gap energy (eV)
0.00	ZnS	21.5	3.45
0.10	ZnS	8.2	3.39
0.30	ZnS	7.0	3.32
	Ni_3S_4	20.9	
0.60	ZnS	3.0	3.16–1.60
	Ni_3S_4	26.4	
	NiS	29.0	
0.80	ZnS	3.0	2.95–1.45
	Ni_3S_4	28.2	
	NiS	33.4	

H_c values were increased due to the formation of the secondary phase of Ni_3S_4 nanocrystals. The bulk Ni_3S_4 is an antiferromagnetic, but in the tetrahedral Ni_3S_4 nanocrystals have a ferromagnetic behavior as the previously reported [49]. In fact, fine particles of an antiferromagnetic material could exhibit magnetic properties such as superparamagnetic and weak ferromagnetism, wherein the permanent magnetic moment can be attributed to an uncompensated number of spins on two sublattices [49, 50]. Secondly, the magnetic properties were decreased with raising Ni^{2+} ions content from 0.4 to 0.8 as the result of formation of NiS nanocrystals as well as undefined microstructures. Tang et al. reported
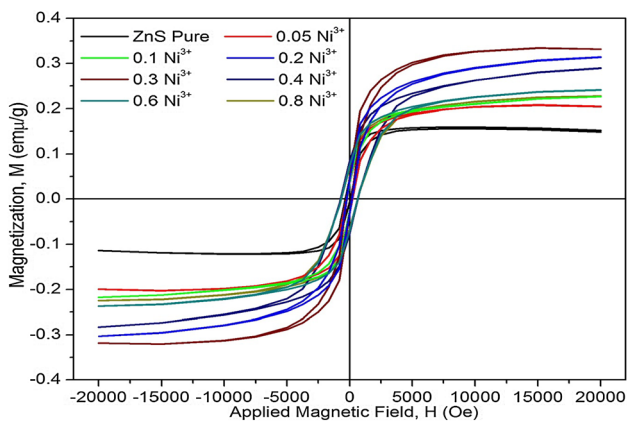
that the magnetic properties of the NiS semiconductor were existence of an obvious hysteretic loop further proves the paramagnetic response of the microstructures in the applied field [46]. Meanwhile, Linganiso et al. [51] indicated that NiS containing two magnetic phases paramagnetic and ferromagnetic ordering; otherwise, since the sample is predominantly NiS nanocrystals, paramagnetic states are prevalent with narrow hysteresis width as well as the slight shift in the loop. This shift has been attributed to a phenomenon called "exchange bias" effect which is observed in nanoscale materials [47–51].

4 Conclusion

Ternary $ZnS/Ni_3S_4/NiS$ nanocomposites have been successfully tailored using hydrothermal strategy based on low-cost chloride salts at low hydrothermal temperature 150 °C for time 24 h and Ni^{2+} ion concentration of 0.40–0.80. Accordingly, the crystallite size for ZnS phase was found to decrease with increasing the Ni^{2+} ion content. Indeed, the crystallite size was decreased from 21.5 nm for pure ZnS to 3.0 nm with further increasing the Ni^{2+} ion molar ratio up to 0.8. The microstructures of pure and substituted ZnS with Ni ion up to 0.6 molar ratios were displayed as microspheres. However, the microspheres transformed to the layers in three dimensions with aggregation of Ni ion with further increasing the Ni^{2+} content up to 0.8. The optical reflectivity of pure ZnS was evinced to be around 75–78% in the infrared and visible regions, whereas it was being around 35–13% for Ni-substituted ZnS with 0.1 and 0.8 molar ratios. The band-gap energy

Table 3 Magnetic properties of Ni^{2+} substituted ZnS nanoparticles at different Ni^{2+} concentrations from 0.0 to 0.80 hydrothermally treated at temperature 150 °C for time 24 h

Ni ions doped	Phases	Magnetic properties			
		Saturation magnetization, M_{max} (emu/g)	Remanence magnetization, M_r ($10^{-3} \times$ emu/g)	Coercivity, H_c (Oe)	Remanence ratio, M_r/M_s
0.00	ZnS	0.14	24.3	189.2	0.17
0.05	ZnS	0.16	27.9	189.4	0.17
0.10	ZnS	0.19	24.6	178.2	0.13
0.20	ZnS Ni$_3$S$_4$	0.31	35.3	202.8	0.11
0.30	ZnS Ni$_3$S$_4$	0.33	37.2	181.0	0.11
0.40	ZnS Ni$_3$S$_4$ NiS	0.28	77.7	696.6	0.27
0.60	ZnS Ni$_3$S$_4$ NiS	0. 24	71.0	661.5	0.30
0.80	ZnS Ni$_3$S$_4$ NiS	0.23	67.2	663.3	0.30

Fig. 6 M–H hysteresis loops of Ni^{2+} substituted ZnS nanoparticles at different Ni^{2+} concentrations from 0.0 to 0.80 hydrothermally treated at temperature 150 °C for time 24 h

was decreased from 3.39 to 3.32 eV with the incorporating of the Ni content from 0.0 to 0.3. Additionally, the optical band-gap energy was doubled to be 3.16–1.60 and 2.95–1.45 eV for Ni^{2+} ion 0.6 and 0.8 molar ratios, respectively, owing to produce of ZnS/Ni$_3$S$_4$/NiS nanocomposites. Photoluminescence spectra studies described that pure and Ni ion-substituted ZnS (0.1 and 0.2 molar ratios) were observed three emission bands in the ranges of strong UV emission peak 350–375 nm with the slight UV emission peak 375–387 nm and the broadband visible emission at 400–600 nm. Magnetic properties were increased with increasing the Ni^{2+} content up to 0.3 as the result of

the formation of Ni$_3$S$_4$ phase as well as the spin polarization, whereas it was decreased with further increasing the Ni ion concentration from 0.4 to 0.8 because of creating NiS as a third phase and irregular microstructure. Overall, these optical and magnetic investigations evidences to recommend the nanocomposites as the good candidates for the optoelectronics devices applications.

References

1. S. Kumar, N. Kumari, S. Kumar, S. Jain, N. Verma, Appl. Nanosci. **2**(4), 437–443 (2012)
2. F. Gao, J. Zhao, K. Wu, J. Wuhan Univ. Technol. Mater. Sci. Ed. **25**(5), 770–773 (2010)
3. M. Rashad, D. Rayan, A. Ramadan, J. Mater. Sci. Mater. Electron. **24**(8), 2742–2749 (2013)
4. M. Rashad, S. Soltan, A. Ramadan, M. Bekheet, D. Rayan, Ceram. Int. **41**(9), 12237–12245 (2015)
5. M. Rashad, D. Rayan, K. El-Barawy, J. Phys. Conf. Ser. **200**(7), 072077 (2010)
6. J.D. Bryan, D.R. Gamelin, Prog. Inorg. Chem. **54**, 47–126 (2005)
7. C.-C. Chen, Y.-J. Hsu, Y.-F. Lin, S.-Y. Lu, J. Phys. Chem. C **112**(46), 17964–17968 (2008)
8. D.A. Bussian, S.A. Crooker, M. Yin, M. Brynda, A.L. Efros, V.I. Klimov, Nat. Mater. **8**(1), 35 (2009)
9. S.C. Erwin, L. Zu, M.I. Haftel, A.L. Efros, T.A. Kennedy, D.J. Norris, Nature **436**(7047), 91 (2005)
10. D.J. Norris, A.L. Efros, S.C. Erwin, Science **319**(5871), 1776–1779 (2008)
11. H. Kim, W. Sigmund, J. Cryst. Growth **255**(1–2), 114–118 (2003)

12. H. Chen, C. Chen, J. Magn. Magn. Mater. **330**, 66–71 (2013)
13. S.H. Yu, M. Yoshimura, Adv. Mater. **14**(4), 296–300 (2002)
14. T. Charinpanitkul, A. Chanagul, J. Dutta, U. Rungsardthong, W. Tanthapanichakoon, Sci. Technol. Adv. Mater. **6**(3–4), 266–271 (2005)
15. M.A. Malik, N. Revaprasadu, P. O'Brien, Chem. Mater. **13**(3), 913–920 (2001)
16. W. Liu, Mater. Lett. **60**(4), 551–554 (2006)
17. S. Pan, X. Liu, J. Solid State Chem. **191**, 51–56 (2012)
18. Y. Li, Y. Ding, Y. Zhang, Y. Qian, J. Phys. Chem. Solids **60**(1), 13–15 (1999)
19. A.K. Verma, T.B. Rauchfuss, S.R. Wilson, Inorg. Chem. **34**(11), 3072–3078 (1995)
20. J.S. Hu, L.L. Ren, Y.G. Guo, H.P. Liang, A.M. Cao, L.J. Wan, C.L. Bai, Angew. Chem. **117**(8), 1295–1299 (2005)
21. T.I. Chanu, D. Samanta, A. Tiwari, S. Chatterjee, Appl. Surf. Sci. **391**, 548–556 (2017)
22. H.R. Pouretedal, A. Norozi, M.H. Keshavarz, A. Semnani, J. Hazard. Mater. **162**(2–3), 674–681 (2009)
23. M. Godlewski, A. Wójcik-Głodowska, E. Guziewicz, S. Yatsunenko, A. Zakrzewski, Y. Dumont, E. Chikoidze, M. Phillips, Opt. Mater. **31**(12), 1768–1771 (2009)
24. P. Sakthivel, S. Muthukumaran, Opt. Laser Technol. **103**, 109–117 (2018)
25. P. Kaur, S. Kumar, C.-L. Chen, K.-S. Yang, D.-H. Wei, C.-L. Dong, C. Srivastava, S. Rao, Mater. Chem. Phys. **186**, 124–130 (2017)
26. E. Shah, J.V. Vaghasiya, S.S. Soni, C. Panchal, P.S. Suryavanshi, M. Chavda, H.P. Soni, J. Environ. Chem. Eng. **4**(4), 4708–4718 (2016)
27. M.M. Rashad, A.G. Mostafa, B.W. Mwakikunga, D.A. Rayan, Appl. Phys. A **123**(1), 42 (2017)
28. M. Rashad, A. Hassan, A. Nassar, N. Ibrahim, A. Mourtada, Appl. Phys. A **117**(2), 877–890 (2014)
29. A.M. Nassar, E.F. Abo Zeid, A.M. Elseman, N.F. Alotaibi, New J. Chem. **42**(2), 1387–1395 (2018)
30. M. Rashad, A. Ibrahim, D. Rayan, M. Sanad, I. Helmy, Environ. Nanotechnol. Monit. Manag. **8**, 175–186 (2017)
31. M. Rashad, A. Mostafa, D. Rayan, J. Mater. Sci. Mater. Electron. **27**(3), 2614–2623 (2016)
32. M. Rashad, I. Ibrahim, Mater. Technol. **27**(4), 308–314 (2012)
33. M. Rashad, D. Rayan, A. Turky, M. Hessien, J. Magn. Magn. Mater. **374**, 359–366 (2015)
34. A.M. Hassan, A.M. Nassar, N.M. Ibrahim, A.M. Elsaman, M.M. Rashad, J. Coord. Chem. **66**(24), 4387–4398 (2013)
35. L. Roa, A. Vincent, N. Joshi, J. Phys. Chem. Solids **53**(2), 261–265 (1992)
36. D. Rayan, Y. Elbashar, M. Rashad, A. El-Korashy, J. Non Cryst. Solids **382**, 52–56 (2013)
37. A.M. Elseman, M.M. Rashad, A.M. Hassan, ACS Sustain. Chem. Eng. **4**(9), 4875–4886 (2016)
38. M.M. Rashad, A.M. Elseman, A.M. Hassan, Optik. **127**(20), 9775–9787 (2016)
39. A. Elseman, A. Shalan, M. Rashad, A. Hassan, Mater. Sci. Semicond. Process. **66**, 176–185 (2017)
40. J.K. Salem, T.M. Hammad, R.R. Harrison, J. Mater. Sci. Mater. Electron. **24**(5), 1670–1676 (2013)
41. K.J. Kim, Y.R. Park, J. Appl. Phys. **96**(8), 4150–4153 (2004)
42. A. Ubale, A. Bargal, Mater. Res. Bull. **46**(7), 1000–1010 (2011)
43. C. Gervas, S. Mlowe, M.P. Akerman, I. Ezekiel, T. Moyo, N. Revaprasadu, Polyhedron **122**, 16–24 (2017)
44. S. Mehta, S. Kumar, M. Gradzielski, J. Colloid Interface Sci. **360**(2), 497–507 (2011)
45. M. Wu, Z. Wei, W. Zhao, X. Wang, J. Jiang, J. Nanomater. 2017 (2017)
46. H. Tang, G. Xu, L. Weng, L. Pan, L. Wang, Acta Mater. **52**(6), 1489–1494 (2004)
47. W. Zhao, Z. Wei, L. Zhang, X. Wu, X. Wang, J. Jiang, J. Alloys Compd. **698**, 754–760 (2017)
48. T. Kennedy, E. Glaser, P. Klein, R. Bhargava, Phys. Rev. B **52**(20), R14356 (1995)
49. Q. Liu, A. Díaz, A. Prosvirin, Z. Luo, J.D. Batteas, Nanoscale **6**(15), 8935–8942 (2014)
50. C. Tang, C. Zang, J. Su, D. Zhang, G. Li, Y. Zhang, K. Yu, Appl. Surf. Sci. **257**(8), 3388–3391 (2011)
51. E.C. Linganiso, B.W. Mwakikunga, N.J. Coville, S.D. Mhlanga, J. Alloys Compd. **629**, 131–139 (2015)